Silicon Photonic Crystal Modulators for High-Speed Transmission and Wavelength Division Multiplexing

Yosuke Hinakura, Daichi Akiyama, Hiroyuki Ito, and Toshihiko Baba, *Member, IEEE*

(*Invited paper*)

Abstract—**For next-era optical interconnects in data centers, development of compact, energy-efficient, low-cost, and high-speed optical transceivers are required, for which high-performance external modulators in silicon photonics will be key components. We present a silicon photonic crystal waveguide slow light Mach-Zehnder modulator suitable for this purpose. The enhancement in the modulation efficiency via the slow light effect reduces the halfwave voltage-length product $V_\pi L$, maintaining a wide working spectrum over 15 nm. The frequency response of the slow light modulator is constricted by an electrooptic phase mismatch between slow light and RF signals. In this study, this was dramatically improved by matching the phase using meanderline electrodes that delay RF signals. The cutoff frequency was experimentally evaluated to be 32−38 GHz. Using this device, we demonstrated high-speed modulation, including 64-Gbps on-off keying, 100-Gbps pulse amplitude modulation, and 50-Gbps/ch wavelength division multiplexing in 170–200-μm-long devices.**

Index Terms—**Si photonics, modulator, slow light, photonic crystal, wavelength-division multiplexing (WDM)**

I. Introduction

Data centers have become the main point of infrastructure for information and communication technology (ICT) services, for example, cloud storage, social networking, and video streaming. However, the growth of data centers has led to increasing load on three key resources. The first one is the increasing power consumption, where each data center can consume several megawatts [1]. The second one is increasing data traffic; Cisco estimated global data centers to reach 19.5 Zbytes/year by the end of 2021, while only 6.0 Zbytes/year in 2016 [2]. The third one is the physical upscaling of data centers,

with the need for "hyperscale datacenters" to support heavy amounts of data traffic. Optical interconnects that eliminate energy loss and limited bandwidth problems of metal wiring have become commonly used this decade, with their potential for high capacity at low-cost well investigated.

A 400G Ethernet standard for optical interconnects was approved as IEEE 802.3bs in 2017 [3]. In this standard, the bitrate per channel (symbol rate/lane × bits per symbol) reaches as high as 100 Gbps. In addition, long-reach standards over 2 km are anticipated to be frequently in use due to data center upscaling. Such high speeds and long distances are considered to require low-dispersion single-mode fibers and external electrooptic (EO) modulators as alternatives to current multimode fibers and direct modulation of vertical cavity surface emission lasers. Therefore, high-speed and low power consumption external modulators will be key components. Furthermore, the multi-source agreement (MSA) group standardized the form factor of pluggable transceiver modules for equipment [4]. The form factor of 400G lambda MSA can have a module area per lane of less 225 mm², and is estimated to become smaller in future standards as the optical transceivers shift to mid-board and on-board optics from the current pluggable modules, due to denser connection and shorter electrical transmission lines. Therefore, external modulators also require smaller footprints, not only to reduce power consumption (which is almost proportional to device length), but also to improve the degree of freedom in layout. In addition, feasibility for low-cost mass production is needed to supply increasing demand. Silicon (Si) photonics provides an attractive platform for such next-era optical interconnects because of the capability for dense photonic integration and low-cost mass production.

Si external modulators under current development, based on carrier plasma dispersion (CPD), are classified into microring modulators (MRMs) [5–8] and Mach-Zehnder modulators (MZMs) [9–15]. MRMs which exploit optical resonance are very compact; the radius of the microring is usually < 10 μm and consumes a low bit energy of order 10 fJ. However, because the working spectrum is as narrow as several tens of picometers, MRMs need a precise temperature controller for stable operation [8], leading to increased total power consumption and implementation cost. In contrast, MZMs

D. Akiyama was with the Department of Electrical and Computer Engineering, Yokohama National University, Yokohama 240–8501, Japan. He is now with Fujitsu Frontech, Inc.

Y. Hinakura, H. Ito, and T. Baba are with the Department of Electrical and Computer Engineering, Yokohama National University, Yokohama 240–8501, Japan (e-mail: hinakura-yosuke-zm@ynu.jp; ito-hiroyuki-tw@ynu.ac.jp; baba-toshihiko-zm@ynu.ac.jp)
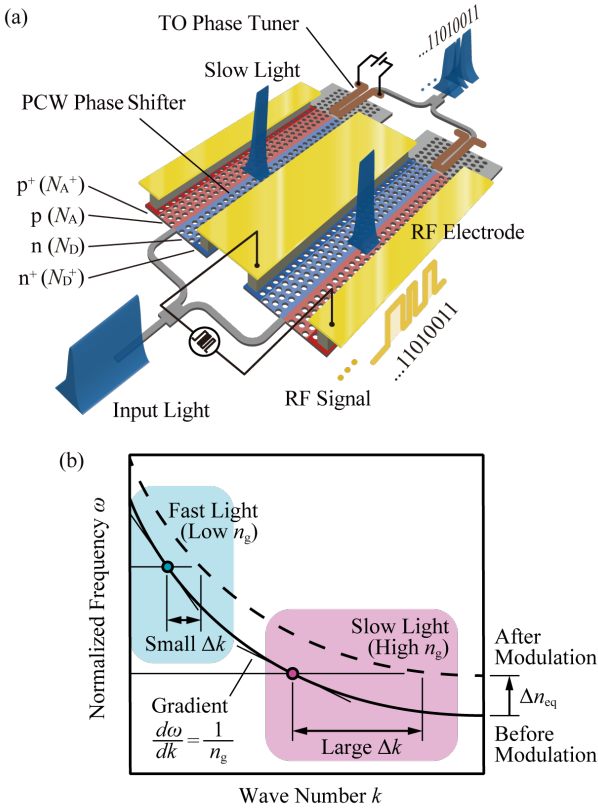
Fig. 1 (a) Schematic of Si PCW MZM. (b) Principle of slow light enhancement.

operate stably over a wide spectrum, and high speeds have been demonstrated; 90-Gbps on-off keying (OOK) and 128-Gbps pulse amplitude modulation (PAM) in a substrate-removed Si modulator were reported recently with a halfwave voltage-length product $V_\pi L$ of 1.4 V·cm [15]. As understood from this value of $V_\pi L$, Si MZMs still need several millimeter phase shifters for operation under complementary-metal-oxide-semiconductor (CMOS) compatible voltage. Recently, hybrid modulators on Si, for instance, Si-organic [16] and III-V/Si [17] were studied for a reduction in $V_\pi L$. While hybrid integration showed the potential for $V_\pi L < 0.1$ V·cm owing to its superb material properties, we can assume a long developing period will be necessary to establish cost-effective fabrication and verify reliability. Therefore, a pure CMOS-compatible Si compact modulator with a wide working spectrum is desirable for the next working standard.

We have studied Si photonic crystal waveguide (PCW) MZMs [18–21], illustrated in Fig. 1(a); the PCW generates slow light, which enhances the modulation efficiency in a short L of several hundred microns, maintaining a sufficient working spectrum. In this paper, after outlining the fundamental concept and fabrication process of this device, we present the latest results, i.e., an improved frequency response, 64-Gbps OOK and 100-Gbps PAM modulations, and 50-Gbps/ch in a wavelength division multiplexing (WDM) circuit.

II. PHOTONIC CRYSTAL MODULATOR

Slow light in the PCW has a small group velocity v_g and

corresponding large group index n_g. The CPD-induced phase shift $\Delta\phi$ in a phase shifter of the Si PCW MZM is expressed as

$$\Delta\phi = \Delta k L = k_0 n_g \frac{\Delta n_{eq}}{n_{eq}} \zeta L , \quad \zeta \equiv \frac{n_{eq}}{\omega_b} \frac{d\omega_b}{dn_{eq}} \qquad (1)$$

where Δk is the shift of the wavenumber, k_0 is the wavenumber in vacuum, n_{eq} is the modal equivalent index, Δn_{eq} is the change of n_{eq} by the modulation, and ω_b is the angular frequency of light. Eq. (1) shows that $\Delta\phi$ is proportional to n_g, and this effect is further explained in Fig. 1(b). Δn_{eq} shifts the photonic band and thus changes k at ω_b. In the fast-light regime with a low n_g, the gradient of the photonic band $d\omega/dk$ is large, resulting in a small Δk. In the slow light regime with a large n_g, the gradient is small, resulting in a large Δk. This large Δk allows for a short L and corresponding small footprint and low power consumption for the same Δn_{eq}. We experimentally observed the slow light enhancement in proportion to n_g with an estimated $V_\pi L$ of 0.18 V·cm for $n_g = 57$ [20]. The typical length L we employed was 200 μm.

Furthermore, photonic band engineering via structural tuning allows the band to become straight so that group velocity dispersion is suppressed. Our group reported low-dispersion (LD) slow light with $n_g \approx 20$ and bandwidth $\Delta\lambda \approx 16$ nm generated in a third-row lattice-shifted PCWs (LSPCWs) [22, 23]. By using this structure, the wavelength range was confirmed in the modulator [20] with a wide temperature tolerance of 19°C–124°C also demonstrated [18].

III. EO PHASE MATCHING

Previously, the bitrate of the PCW MZM was limited to up to 32 Gbps, although the RC time constant of the phase shifter was improved by optimizing the p-n doping [19]; the EO phase mismatch affected the frequency response [20, 21]. Because of the high $n_g > 20$ of slow light, the PCW MZM behaves as a traveling-wave modulator [20–23] even for $L \leq 200$ μm, and therefore the large difference in n_g between slow light and ~4 for RF signals causes EO phase mismatch and degrades the frequency response. To solve this problem, we introduced meanderline electrodes at the center of the phase shifters, as shown in Fig. 2, which delay the RF signals in the length L_d and compensate for the phase mismatch. In the first half section of the phase shifter, the slow light and RF signals copropagate while displacement increases gradually, as shown in Fig. 2(a). In the second half, the RF signal copropagates with slow light after a delay, as shown in Fig. 2(b). A similar EO phase matching scheme was reported for a III-V compound semiconductor MZM [26]. In comparison to this, our slow light MZM requires a much longer L_d of around 1 mm.

IV. DESIGN, FABRICATION, AND OPERATION

Fig. 3(a) shows a device fabricated by a CMOS process using a KrF excimer laser at $\lambda = 248$ nm for stepper exposure on 200-mm-diameter silicon-on-insulator (SOI). With this matured process, the yield of the device described below was almost 100%, although the operating wavelength had a
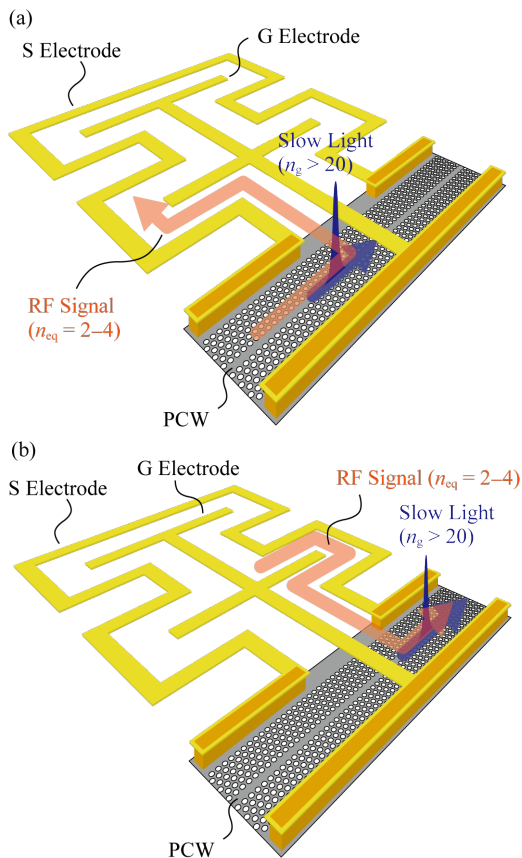
Fig. 2 EO phase matching via meanderline electrode. Copropagating slow light and RF signals in (a) the first half section of the phase shifter, and (b) the second section.
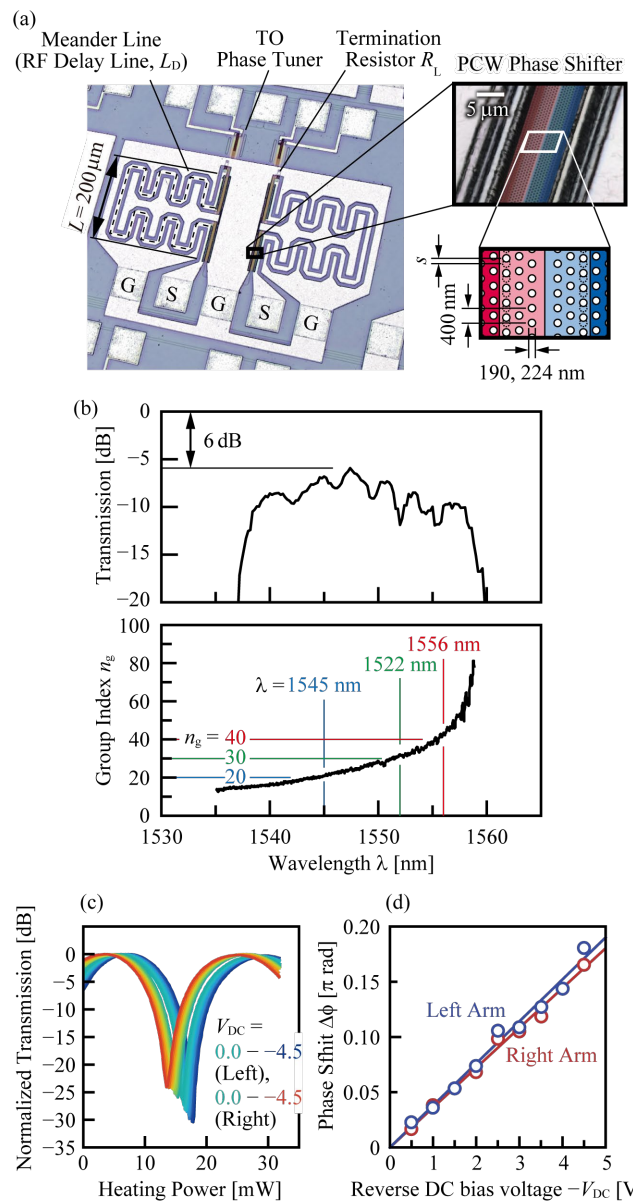

Fig. 3 (a) Fabricated meanderline device with $L_d = 1168$ μm. Insets show a magnified view and schematic of PCW. (b) Optical transmission and n_g spectra measured for a device in Lot #1. (c) Normalized optical transmission for heating power when V_{DC} was changed. (d) $\Delta\phi$ for $-V_{DC}$.

nonuniformity of ±0.2% over the wafer, which corresponds to wavelength shifts of ±3 nm at the telecom wavelengths. The nonuniformity between wafers in the same lot was comparable, but that at different lots was as large as ±1%. It might be caused by the fluctuations in the diameter of holes of the PCW and in the thickness of the Si slab, which should be suppressed in future studies. In the following, we describe the wafers of two different lots: Lot #1 with Si slab thicknesses $t = 210$ nm and Lot #2 with $t_{Si} = 205$ nm. The devices in Lot #1 and #2 were used in the experiments in Section V−VII and Section VIII, respectively. For the stepper exposure, phase shift masks were particularly used for the Si and photonic crystal layers to enhance the resolution to < 130 nm. The Si PCWs consisted of a line defect in triangular-lattice arrays of holes with lattice constant a and diameter $2r$ buried in the SiO_2 cladding, as shown in the insets of Fig. 3(a). We set $L = 200$ μm, $a = 400$ nm and $2r = 190$ nm in Lot #1 and $L = 170$ μm, $a = 404$ and 407 nm, and $2r = 224$ nm in Lot #2. Note that these L included 32-μm undoped interval region between the first and second half sections. Therefore, the effective phase shifter length was 168 μm and 138 μm for the devices in Lot #1 and #2, respectively. In this study, we omitted third-raw lattice shifts to obtain a gradually increasing n_g with increase in λ. The linear p-n junction with an accepter concentration $N_A = 1.05 \times 10^{18}$ cm^{-3} and donor concentration $N_D = 6.2 \times 10^{17}$ cm^{-3} was incorporated

in the PCW phase shifters. Each width of the p- and n-doped regions was 2 μm. The heavily p- and n-doped regions of $N_A^+ = N_D^+ = 1.9 \times 10^{19}$ cm^{-3} were prepared outside of the p-n junction for the ohmic contact, which was placed 4 μm apart to avoid strong free-carrier absorption (FCA). A coplanar waveguide (CPW) structure was employed for the RF electrodes; the width of the signal (S) electrodes sandwiched by ground (G) electrodes was 10 μm and the S-G gap was 7 μm. The delay length L_d was set at 0 (a normal electrode), 422, 804, 1186, and 1568 μm in Lot #1 and 370 μm in Lot #2, which were determined in the calculation based on a traveling-wave modulator model [21]. The CPW electrodes were terminated by TiN load resisters $R_L = 20$, 30, 45, 50, and 100 Ω. The value of R_L determines the RF reflectivity Γ_L expressed as

$$\Gamma_L = \frac{R_L - Z_0}{R_L + Z_0} \quad (2)$$

where Z_0 is the characteristic impedance of the phase shifter. Γ_L takes a negative value when $R_L < Z_0$. In the calculation, we estimated that a negative Γ_L emphasizes the response at > 20 GHz and f_{3dB} reached 56 GHz at $\Gamma_L = -0.5$.

Transverse-electric polarized light from a tunable laser was coupled in the device through a polarization maintaining fiber (PMF) with a lens module and a spot size converter (SSC) on the chip. Output light was extracted through another SSC and PMF. Fig. 3(b) shows the optical transmission and n_g spectra measured for $t = 210$ nm, $L = 200$ μm, $a = 400$ nm, $2r = 190$ nm, $L_d = 1186$ μm, and $R_L = 30$ Ω. The n_g increased gradually with increase in λ; the device exhibited $n_g = 12$ and 81 at λ = 1535 nm and 1559 nm, respectively. The shortest λ corresponds to a cross point between the photonic band of the slow light mode and SiO$_2$ light line, and the longest λ corresponds to the band edge of the mode. We changed n_g by shifting λ and set $n_g = 20$, 30, and 40 at λ = 1545, 1552, and 1556 nm, respectively. The on-chip optical insertion loss was 6 dB at λ = 1547.4 nm for n_g = 24; this loss was composed of (i) coupling losses between the PCW and Si wire input/output waveguides of ~1.5 dB in total, (ii) excess losses at the 1 × 2 multimode interference splitter and combiner of < 0.5 dB in total, (iii) propagation loss in the PCW of ~4 dB for $n_g = 24$. This propagation loss was 1 dB larger than a previously reported value for $n_g = 20$ [20] because of the slightly higher n_g. The loss increased at shorter λ because the mode penetrated more deeply into the photonic crystal in which the FCA absorption in heavy-doped regions increased. The loss increased at longer λ also due to the increased scattering and FCA losses by the higher n_g. The latter can be suppressed by employing LSPCW which generates LD slow light.

We measured the DC modulation characteristics of the PCW phase shifters in another device sample of the same design. Fig. 3(c) shows the transmission as a function of the heating power for TiN thermo-optic (TO) phase tuners, which were formed on both left and right arms in the MZM, as shown in Fig. 3(a). Here, we set $n_g = 20$ and changed the bias voltage V_{DC} for the phase shifters. The sinusoidal response was obtained for the heating power and it was shifted by V_{DC}. From this shift, we estimated Δϕ, as shown in Fig. 3(d); Δϕ = 0.17π–0.18π at V_{DC} = −4.5 V. Using this value and the effective phase shifter length of 168 μm, we evaluated $V_\pi L = 0.44$ V·cm on average .

V. FREQUENCY RESPONSE

We measured the EO frequency response of the devices using a vector network analyzer (Anritsu, 37269A). This is shown in Fig. 4(a) for $R_L = 50$ Ω and different L_d at $V_{DC} = -2$ V. Longer L_d improved the response for both $n_g = 20$ and 40, but it was clearest at $n_g = 40$. Fig. 4(b) summarizes the estimated cutoff frequency f_{3dB}. For $n_g = 20$, f_{3dB} was 19 GHz for $L_d = 0$ and improved to > 30 GHz for $L_d = 1186$ μm. Even for $n_g = 30$ and 40, f_{3dB} was improved to ~30 GHz. We also measured the response for different R_L with $L_d = 1186$ μm; Fig. 5(a) shows
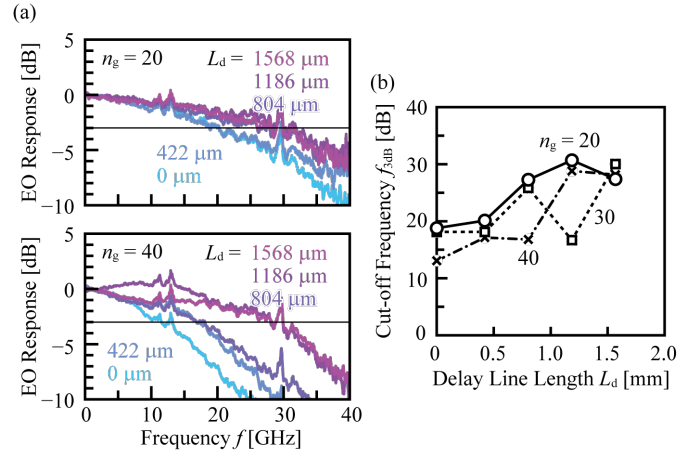

Fig. 4 (a) Measured EO response of 50-Ω terminated devices for $V_{DC} = -2$ V and different L_d. (b) f_{3dB} of the EO response as a function of L_d.
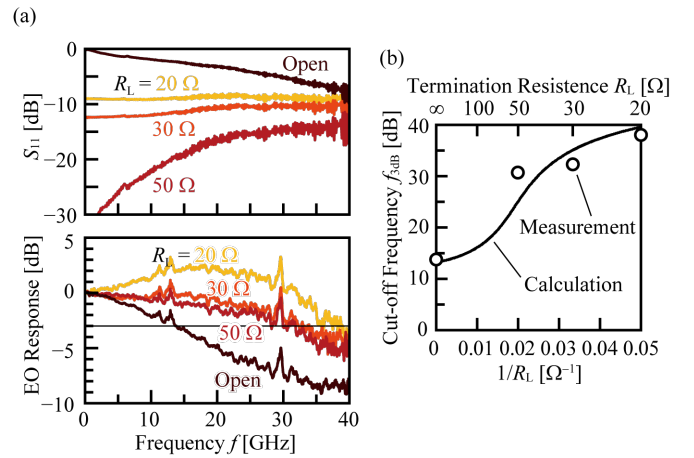

Fig. 5 (a) Measured S_{11} and EO response of meanderline devices for $V_{DC} = -2$ V and different R_L. (b) f_{3dB} of the EO response as a function of 1/ R_L.

the measured S_{11} (RF reflection) and EO response. The open-terminated device exhibited $S_{11} > -10$ dB over the measured frequency range. When the device was terminated by $R_L = 50$ Ω, S_{11} was reduced to < −14 dB. It increased again for $R_L = 20$ Ω and 30 Ω, indicating that R_L was less than Z_0 and Γ_L was a negative value. The EO response with a load resistor was much improved compared to the open device. In particular, improvement was remarkable for $R_L = 20$ Ω. Fig. 5(b) summarizes f_{3dB} as a function of $1/R_L$. The measured f_{3dB} was in rough agreement with the calculated curve. Therefore, the calculation modeled the meanderline device well. The f_{3dB} was improved to 38 GHz for $R_L = 20$ Ω, which was capable of high-speed operation beyond 40 Gbps.

VI. HIGH-SPEED OOK

We performed modulation at 50, 56, and 64 Gbps in the meanderline device with $L_d = 1186$ μm and $R_L = 20$ Ω using the measurement setup in Fig. 6. The non-return-to-zero (NRZ) pseudo-random binary sequence (PRBS) signals were generated using a 2:1 multiplexer (MUX, SHF 601 A), frequency doubler (SHF 1428 A), and equalizer (EQ, SHF EQ25A) added to a pulse pattern generator (PPG, Anritsu MP1800A). Two-channel 25-, 28-, or 32-Gbps signals of
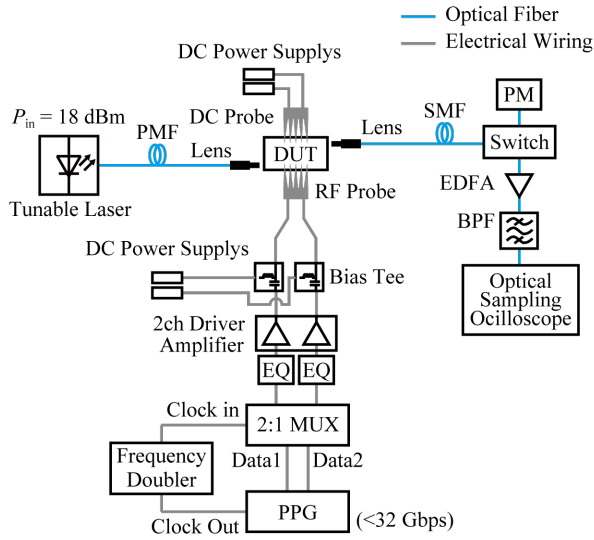
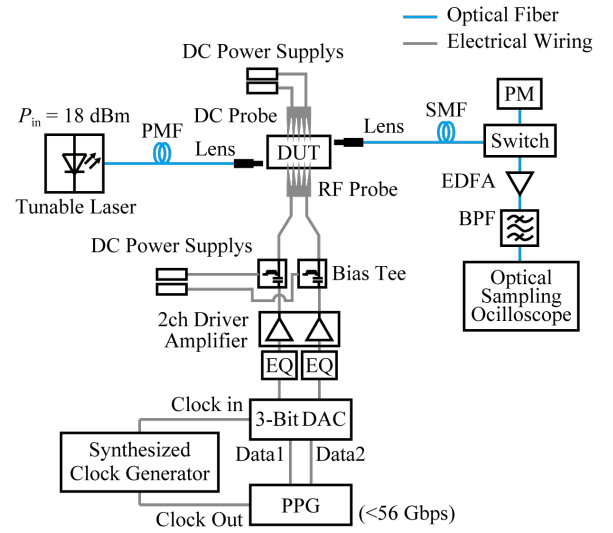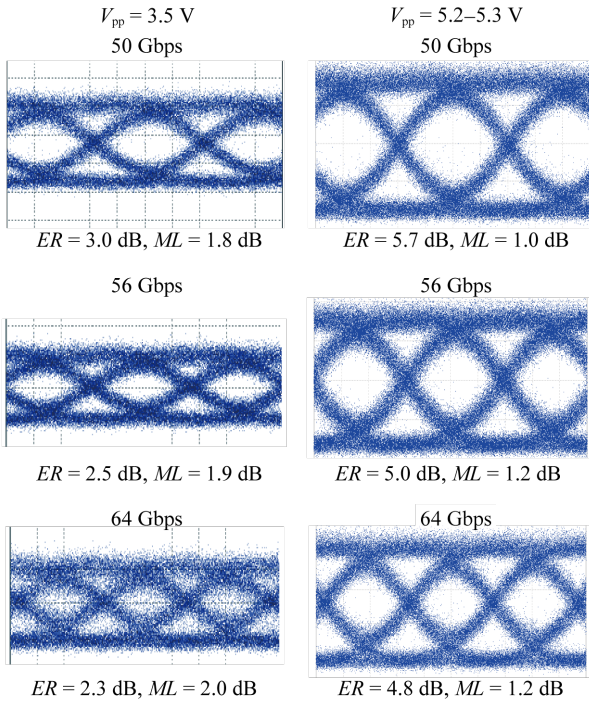Fig. 6 Measurement setup for 50-, 56-, 64-Gbps OOK modulation.

Fig. 8 Measurement setup for PAM4 modulation.

Fig. 7 Eye patterns for the modulation at 50-, 56-, 64-Gbps in 20-Ω terminated meanderline device with $n_g = 20$, $V_{pp} = 3.5$, 5.2–5.3 V and $V_{DC} = -3$ V.

different bit lengths were sent from the PPG to the MUX with clock signals at a frequency $f_{clk} = 12.5$, 14, or 16 GHz of the PPG after the frequency doubled. Thus, 50-, 56-, or 64-Gbps signals were generated. They were amplified by RF amplifiers (SHF S804 B, $f < 60$ GHz, or Alnair Labs DRV-400, $f < 40$ GHz), and the data and data-bar signals were applied to the GSGSG electrodes on the device to perform push-pull drive. Modulated light was evaluated by an asynchronous sampling oscilloscope (Alnair Labs, EYE-1000C) after passing through an erbium-doped fiber amplifier (EDFA) and a tunable bandpass filter (BPF).

Fig. 7 shows the observed eye patterns at $V_{pp} = 2.7$, 3.5,

5.2–5.3 V and $V_{DC} = -3$ V when the initial phase difference ϕ_0 between two arms of the MZM was set at $\pi/2$. At drive voltage $V_{pp} = 3.5$ V, the extinction ratio ER was observed to be 3.0, 2.5, and 2.3 dB at 50, 56, and 64 Gbps, respectively. A clear open eye was observed at 50 and 56 Gbps, although it became noisy at 64 Gbps because of the unstable self-trigging of the used oscilloscope. The excess optical loss under modulation, referred to as ML here, was estimated to be 1.8, 1.9, and 2.0 dB from the measured ER and $\phi_0 = \pi/2$. When V_{pp} was increased to 5.2–5.3 V, we observed a clear open eye with a high ER of 5.7, 5.0, and 4.8 dB at 50, 56, and 64 Gbps, respectively. From these eye patterns at 50, 56, and 64 Gbps, a bit error rate BER of 8.9×10^{-9}, 4.7×10^{-7}, and 2.8×10^{-5} was estimated, respectively.

VII. PULSE AMPLITUDE MODULATION

We attempted to demonstrate 20–50-Gbaud PAM4 modulation using the setup in Fig. 8. The PAM4 signals were generated by a 3-bit digital-to-analog convertor (DAC), 128-Gbps PPG (SHF 12103A, 56 Gbps/ch), and synthesized clock generator (SHF 78122B). The DAC generated 20–50 Gbaud PAM4 signals according to two-channel 20–50 Gbps PRBS signals from the PPG; the signals were synchronized with the clock generator. The PAM4 signals were applied to the device after amplification to $V_{pp} = 2.9$ or 3.1 V (depending on the symbol rate) using SHF S804 B with a high linearity. We used the same device as that in Section VI; $R_L = 20$ Ω and $L_d = 1186$ µm. Fig. 9(a) shows the PAM-4 eye patterns and their amplitude histograms in the decision ranges for $n_g \approx 20$, $\phi_0 = \pi/2$, and $V_{DC} = -3$ V. We defined the width of the decision range as the one fourth of a symbol. The open eye patterns were observed for symbol rates of up to 28 Gbaud. The pitch of the four-level amplitudes was slightly unequal because of the nonlinearity of the device. Although the eye pattern became noisier with increase in the symbol rate, we barely observed the opened eye even at 50 Gbaud, which corresponded to 100 Gbps. We estimated the BER from the histograms fitted with four
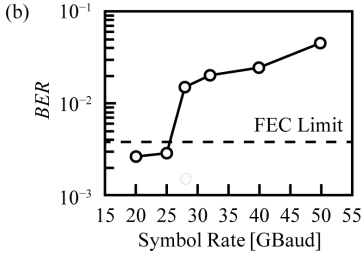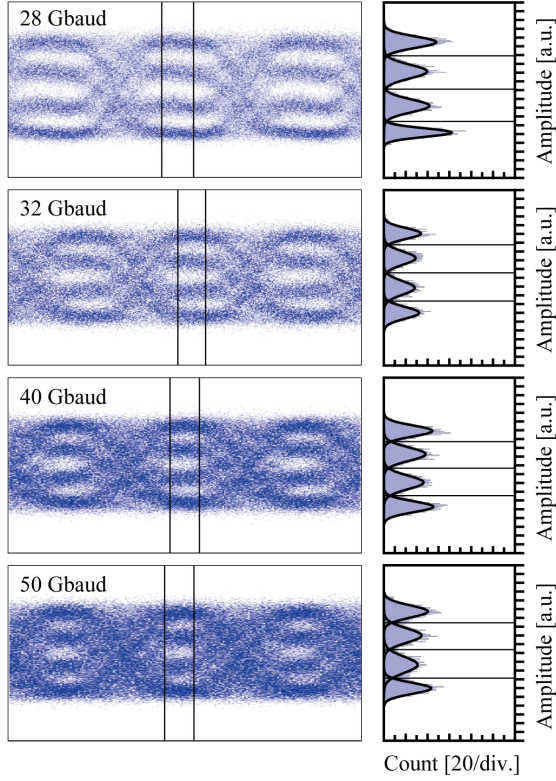
Fig. 9 (a) PAM4 eye patterns modulated by 20-Ω terminated meanderline device for $n_g = 20$, $V_{pp} = 3.1$ V and $V_{DC} = -3$ V.

Gaussian curves, from which we obtained the number of symbols and each overlapped area. Fig. 9(b) summarizes the *BER* estimated for the symbol rate. The *BER* was below the forward error correction limit of 3.8×10^{-3} [27] up to 25 Gbaud, but exceeded 10^{-2} at higher symbol rates. In PAM-4 operation, 1.5-fold f_{3dB} is required from the symbol rate. In this study, the frequency equalization was only applied to the measurement system. Further improvement is expected by adding the equalization of the device.

VIII. WAVELENGTH DIVISION MULTIPLEXING

We performed a WDM transmission experiment using two meanderline PCW MZMs of $R_L = 45$ Ω and an optical MUX device in another Si photonics chip. Here we used the devices in Lot #2, where $L = 170$ μm and $L_d = 370$ μm. The two different aforementioned a were used for different operation wavelengths. In general, a shorter L offers a higher f_{3dB} for the same R_L. As shown in Fig. 4(b), the $L = 200$ μm device exhibited $f_{3dB} = 32$ GHz for $R_L = 50$ Ω. Therefore, the device in this experiment having shorter L and smaller R_L was expected
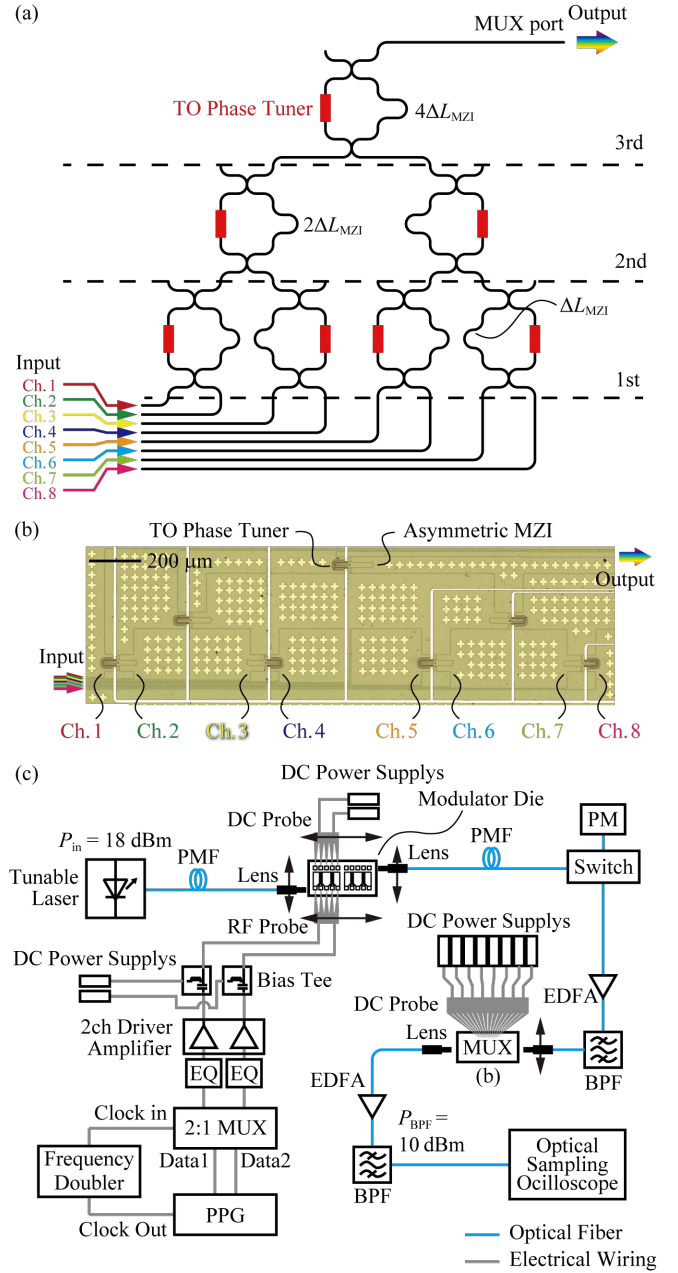

Fig. 10 (a) Schematic of optical MUX consisting of asymmetric Mach-Zehnder interferometers. (b) Top view of fabricated MUX. (c) Setup for WDM transmission experiment using Si PCW modulators and MUX.

to show f_{3dB} higher than 32 GHz.

Figs. 10(a) and (b) show the schematic and an optical micrograph of the eight-channel optical MUX. It consisted of a three-stage tournament tree of 2×2 asymmetric Mach-Zehnder interferometer (MZIs), each having a TO phase tuner to compensate for the initial phase offset and showing a sinusoidal response with λ. The single switch had a tuned waveguide of 225.7 μm length. The length of the reference waveguide was different from the tuned waveguide's by ΔL_{MZI}. The free spectral range *FSR* is given as $\lambda^2/n_g \Delta L_{MZI}$. Assuming λ = 1.55 μm and $n_g = 4.5$, ΔL_{MZI} in the third stage switch was determined to be 55.87 μm, which corresponded to *FSR* = 10 nm. At the
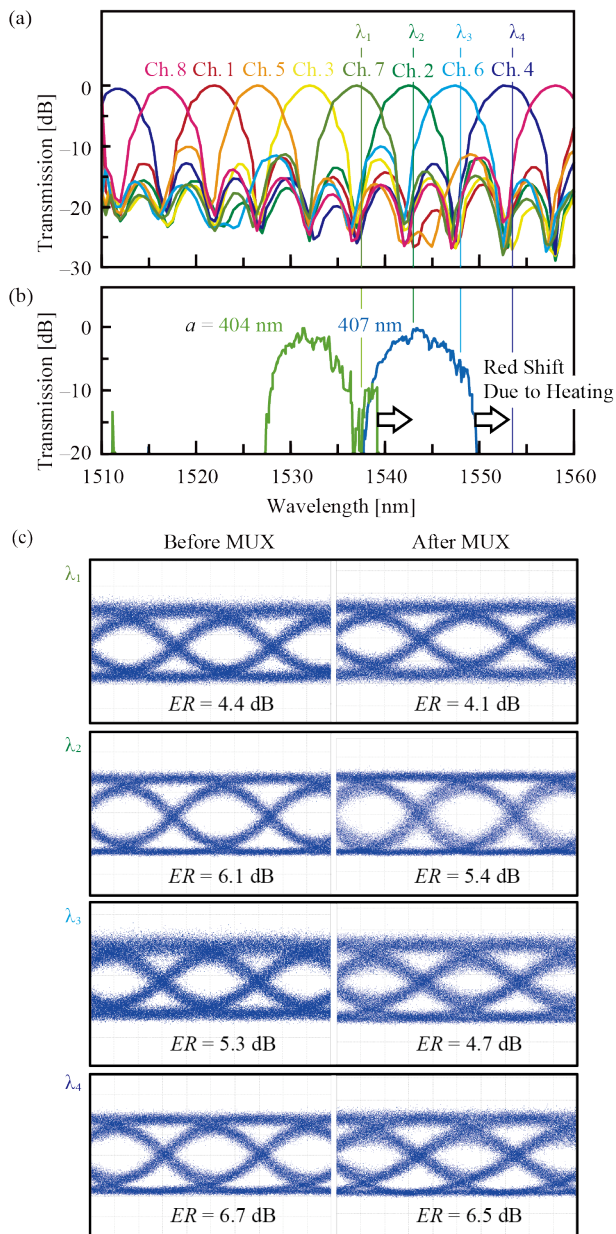
Fig. 11 Measurement results of WDM transmission experiment. (a) Transmission spectra of MUX and (b) that of the Si PCW modulators fabricated in Lot #2. (c) 50-Gbps eye patterns before/after the multiplexing.
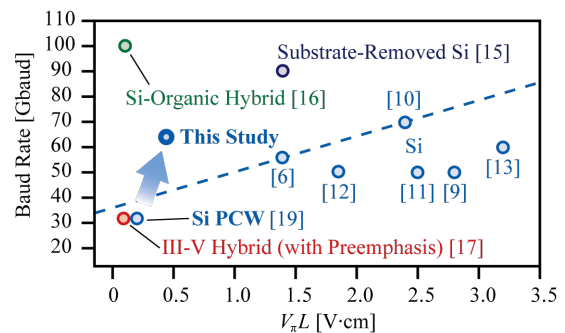

Fig. 12 Benchmarking of MZMs on SOI and the device in this study.

Fig. 11(a) shows the normalized transmission spectrum of the eight-channel MUX after TO tuning. The transmission spectra were evenly aligned, and the crosstalk was suppressed to −20 dB. Fig. 11(b) shows the normalized transmission spectra of the two meanderline modulators. These originally had transmission bands of λ = 1528–1539 nm and 1539–1549 nm. The bands were redshifted by 5 nm due to heating caused by the relatively high RF power in the phase shifters and DC power in the TO phase tuners. The former effect was not intended, whereas the latter effect was intended to adjust the wavelength to the four transmission wavelengths λ_1–λ_4 of the MUX. Fig. 11(c) shows the observed 50-Gbps eye patterns at these four wavelengths before and after the multiplexing. We observed clear eye patterns for these channels even after the multiplexing. We noted measured ER at each channel, which was affected by the two-step EDFA amplification. Therefore, this observation might exhibit worse performance than an ideal situation where the modulators and MUX are integrated on the same chip. The slight nonuniformity in the eye patterns might also be caused by high dispersion of the PCW without lattice shifts. This is solved by employing LSPCWs for the WDM transmissions. Using LSPCWs, we can choose a higher n_g, e.g., 30, for more efficient modulation. This narrows the transmission bandwidth to < 15 nm, but is not a drawback for WDM transmission where the operation wavelengths are strictly managed.

IX. CONCLUSION

We improved the frequency response of Si PCW MZMs via EO phase matching using meanderline electrodes and demonstrated high-speed modulation at 50−64 Gbps. The fabricated meanderline devices exhibited f_{3dB} > 30 GHz, whereas the normal electrode device exhibited f_{3dB} of 19 GHz. In particular, a maximum f_{3dB} of 38 GHz was obtained for the 20-Ω terminated meanderline device. Using this, 50- and 56-Gbps open eyes were observed for V_{pp} = 3.5 V, and 64-Gbps for V_{pp} = 5.2 V. The V_{pp} values can be reduced, for example to 2.3 and 3.5 V, by employing n_g = 30. In PAM-4 modulation, we observed eye patterns at 20−50 Gbaud (40−100 Gbps); the eye became noisy at 100 Gbps but barely open. In the WDM experiment using an additional MUX chip, 50-Gbps/ch for four channel transmission (potentially 200 Gbps in total) was

first and second stages, ΔL_{MZI} were 13.97 μm and 27.94 μm, so that the FSR became 40 nm and 20 nm, respectively. Figs. 10(c) shows the measurement setup, which was based on the scheme in Fig. 6 but modified for the WDM experiment including the MUX chip. We prepared two meanderline modulators with different a to cover the four wavelength channels of ~15 nm total width. These devices were driven by 50-Gbps NRZ PRBS signals with V_{pp} = 5.3 V and V_{DC} = −3 V. The ϕ_0 was set so that the eye patterns were clearest. Light modulated by these devices was multiplexed in the MUX device after passing through EDFA and BPF to compensate for the coupling loss at SSCs. The final output was observed using the same optical sampling oscilloscope in Figs. 6 and 8.

demonstrated. The number of channels was limited to four due to the PCW design used; using LSPCWs can increase it to eight, allowing 400 Gbps transmission.

Fig.12 shows a benchmark of results from Si MZMs at symbol rates equal to and beyond 50 Gbaud [9–13], hybrid integrated MZMs [16, 17], and this study, where the upper left shows higher performance. The Si MZMs data points range from $V_\pi L$ = 1.6–3.2 V·cm (1.4–3.2 V·cm when the substrate-removed Si MZM [15] is included) and operating symbol rate of 50–70 Gbaud. In our previous study [19], the Si LSPCW MZM with the wavy p-n junction showed 32 Gbaud operation with $V_\pi L$ = 0.2 V·cm. The meanderline PCW MZMs with the linear p-n junctions in this study showed $V_\pi L$ = 0.44 V·cm while improving the symbol rate to up to 64 Gbaud. Therefore, the Si PCW MZM recorded the highest performance among the CMOS-compatible Si MZMs based on these criteria. The above results demonstrate the feasibility of Si LSPCW MZM as a compact, low-cost, high-speed modulator with a wide working spectrum for use in 400 Gbps Ethernet and networks in the next generation of standards.

REFERENCES

[1] K. Kant, "Data center evolution," *Computer Networks*, vol. 53, no. 17, pp. 2939–2965, Dec. 2009.

[2] "Cisco Annual Internet Report," *Cisco Annual Internet Report - Cisco*. https://www.cisco.com/c/en/us/solutions/executive-perspectives/annual-internet-report/index.html#cloud-forecast (accessed Apr. 20, 2020).

[3] "IEEE Standard for Ethernet - Amendment 10: Media Access Control Parameters, Physical Layers, and Management Parameters for 200 Gb/s and 400 Gb/s Operation," *IEEE Std 802.3bs-2017 (Amendment to IEEE 802.3-2015 as amended by IEEE's 802.3bw-2015, 802.3by-2016, 802.3bq-2016, 802.3bp-2016, 802.3br-2016, 802.3bn-2016, 802.3bz-2016, 802.3bu-2016, 802.3bv-2017, and IEEE 802.3-2015/Cor1-2017)*, pp. 1–372, Dec. 2017, doi: 10.1109/IEEESTD.2017.8207825.

[4] "100G Lambda MSA." https://100glambda.com/ (accessed Apr. 20, 2020).

[5] Q. Xu, B. Schmidt, S. Pradhan, and M. Lipson, "Micrometre-scale silicon electro-optic modulator," *Nature*, vol. 435, no. 7040, pp. 325–327, May 2005.

[6] M. Pantouvaki *et al.*, "Active Components for 50 Gb/s NRZ-OOK Optical Interconnects in a Silicon Photonics Platform," *J. Lightwave Technol.*, vol. 35, no. 4, pp. 631–638, Feb. 2017.

[7] J. Sun, R. Kumar, M. Sakib, J. Driscoll, H. Jayatilleka, and H. Rong, "A 128 Gb/s PAM4 silicon microring modulator with integrated thermo-optic resonance tuning," *J. Lightwave Technol.*, vol. 37, no. 1, pp. 110–115, 2019.

[8] H. Jayatilleka *et al.*, "Wavelength tuning and stabilization of microring-based filters using silicon in-resonator photoconductive heaters," *Opt. Express*, vol. 23, no. 19, p. 25084, Sep. 2015.

[9] D. J. Thomson *et al.*, "50-Gb/s Silicon Optical Modulator," *IEEE Photon. Technol. Lett.*, vol. 24, no. 4, pp. 234–236, Feb. 2012.

[10] H. Xu *et al.*, "High-speed silicon modulator with band equalization," *Opt. Lett.*, vol. 39, no. 16, pp. 4839–4842, Aug. 2014.

[11] M. Streshinsky *et al.*, "Low power 50 Gb/s silicon traveling wave Mach-Zehnder modulator near 1300 nm," *Opt. Express*, vol. 21, no. 25, pp. 30350–30357, Dec. 2013.

[12] Y. Yang, Q. Fang, M. Yu, X. Tu, R. Rusli, and G.-Q. Lo, "High-efficiency Si optical modulator using Cu travelling-wave electrode," *Opt. Express*, vol. 22, no. 24, p. 29978, Dec. 2014.

[13] D. Patel *et al.*, "Design, analysis, and transmission system performance of a 41 GHz silicon photonic modulator," *Opt. Express*, vol. 23, no. 11, p. 14263, Jun. 2015.

[14] H. Yu and W. Bogaerts, "An equivalent circuit model of the traveling wave electrode for carrier-depletion-based silicon optical modulators," *J. Lightwave Technol.*, vol. 30, no. 11, pp. 1602–1609, Jun. 2012.

[15] M. Li, L. Wang, X. Li, X. Xiao, and S. Yu, "Silicon intensity Mach–Zehnder modulator for single lane 100 Gb/s applications," *Photon. Res.*, vol. 6, no. 2, p. 109, Feb. 2018.

[16] S. Wolf *et al.*, "Silicon-Organic Hybrid (SOH) Mach-Zehnder modulators for 100 Gbit/s on-off keying," *Sci. Rep.*, vol. 8, no. 1, p. 2598, Dec. 2018.

[17] T. Hiraki *et al.*, "Heterogeneously integrated III-V/Si MOS capacitor Mach-Zehnder modulator," *Nature Photonics*, vol. 11, no. 8., p. 482–485, Aug. 2017.

[18] H. C. Nguyen, N. Yazawa, S. Hashimoto, S. Otsuka, and T. Baba, "Sub-100 μm photonic crystal Si optical modulators: spectral, athermal, and high-speed performance," *IEEE J. Sel. Top. Quantum Electron.*, vol. 19, no. 6, pp. 127–137, Nov. 2013.

[19] Y. Terada, T. Tatebe, Y. Hinakura, and T. Baba, "Si Photonic Crystal Slow-Light Modulators with Periodic p–n Junctions," *J. Lightwave Technol.*, vol. 35, no. 9, pp. 1684–1692, May 2017.

[20] Y. Hinakura, Y. Terada, T. Tamura, and T. Baba, "Wide spectral characteristics of Si photonic crystal Mach-Zehnder modulator fabricated by complementary metal-oxide-semiconductor process," *Photonics*, vol. 3, no. 2, p. 17, Apr. 2016.

[21] Y. Hinakura, H. Arai, and T. Baba, "64 Gbps Si photonic crystal slow light modulator by electro-optic phase matching," *Opt. Express*, vol. 27, no. 10, pp. 14321–14327, May 2019.

[22] Y. Hamachi, S. Kubo, and T. Baba, "Slow light with low dispersion and nonlinear enhancement in a lattice-shifted photonic crystal waveguide," *Opt. Lett.*, vol. 34, no. 7, p. 1072, Apr. 2009.

[23] T. Tamura, K. Kondo, Y. Terada, Y. Hinakura, N. Ishikura, and T. Baba, "Silica-Clad Silicon Photonic Crystal Waveguides for Wideband Dispersion-Free Slow Light," *J. Lightwave Technol.*, vol. 33, no. 14, pp. 3034–3040, Jul. 2015.

[24] M. Izutsu, Y. Yamane, and T. Sueta, "Broad-band traveling-wave modulator using a LiNbO$_3$ optical waveguide," *IEEE J. Quantum Electron.*, vol. 13, no. 4, pp. 287–290, Apr. 1977.

[25] G. L. Li, T. G. B. Mason, and P. K. L. Yu, "Analysis of Segmented Traveling-Wave Optical Modulators," *J. Lightwave Technol.*, vol. 22, no. 7, pp. 1789–1796, Jul. 2004.

[26] Y. Tang, Y. Yu, Y. Ye, U. Westergren, and S. He, "Design and optimization of an arbitrarily segmented traveling wave electrode for an ultrahigh speed electroabsorption modulator," *Opt. Commun.*, vol. 281, no. 20, pp. 5177–5182, Oct. 2008.

[27] A. Leven, F. Vacondio, L. Schmalen, S. ten Brink, and W. Idler, "Estimation of Soft FEC Performance in Optical Transmission Experiments," *IEEE Photon. Technol. Lett.*, vol. 23, no. 20, pp. 1547–1549, Oct. 2011.

Yosuke Hinakura received his B.E, M.E., and Ph.D. Degrees all from the Department of Electrical and Computer Engineering, Yokohama National University, Yokohama, Japan, in 2015, 2017, and 2020, respectively. Then he belonged to NTT laboratories as a researcher. During the Ph.D. studies, he successfully demonstrated high-speed photonic crystal optical modulators. He is a member of the Japan Society of Applied Physics. He received OECC Best Student Paper Award, IEICE LQE Student Presentation Award, and JSAP Presentation Award in 2019.

Daichi Akiyama received his B.E. and M.E. degree from the Department of Electrical and Computer Engineering, Yokohama National University, Yokohama, Japan, in 2018 and 2020, respectively. He studied the photonic crystal modulators for WDM applications. He is now with Fujitsu Frontech, Inc.

Hiroyuki Arai (Fellow) received the B.E. degree in Electrical

and Electronic Engineering, M.E. and D.E.in Physical Electronics from Tokyo Institute of Technology in 1982, 1984 and 1987, respectively. After research associate in Tokyo Institute of technology, he joined Yokohama National University as lecturer in 1989. Now he is professor in Department of Electrical and Computer Engineering, Yokohama National University. He was visiting scholar at university of California, Los Angeles in 1997 and was visiting professor in 2005 and adjunct professor, 2012 -2014, respectively, at Yonsei University, Seoul. He investigated microwave passive components for high power handling applications such as RF plasma heating in large Tokamaks. He developed a flat diversity antenna for mobile telephone terminal, a polarization diversity base station antenna for Japanese PDC systems, small base station antennas of In-building micro cellular system and DOA estimation for cellular system. He received the Young Engineers Award from the IEICE of Japan in 1989 and the "Meritorious Award on Radio" by the Association of Radio Industries and Businesses in 1997 for the development of polarization diversity antenna, in 2006 for the development of DOA estimation system, and in 2011 for the development of light weight phantom. He was editor-in-chief of IEICE Transactions on Communications, 2005 -2007, and was chair of IEEE AP-S Japan Chapter, 2009 - 2010. He was associate editor of IEEE Transactions on Antennas and Propagation, 2011-2013, and chair of Technical Group on Antennas and Propagation of IEICE, 2013-2014. He is Fellow of IEEE and IEICE. He will serve general the chair of ISAP 2020, Osaka, Japan.

Toshihiko Baba (Senior Member) received his B.E., M.E. and Ph.D. degrees all from the Division of Electrical and Computer Engineering, Yokohama National University, Japan, in 1985, 1987 and 1990, respectively. He became an Associate Professor and a Full Professor with Yokohama National University in 1994 and 2005, respectively. He has studied ARROW waveguides, VCSELs, microdisk lasers, photonic crystals (PCs) and Si photonics. His first demonstration includes PC-based slow-light waveguides with the dispersion engineering, high-speed modulators, beam steering device, nanolasers, biosensors and LEDs, and various Si photonics passive components including the sharp bend waveguide and arrayed waveguide grating. He is the author or co-author of more than 200 journal papers. He is a member of IEICE, JSAP, IEEE/Photonics, and OSA, and an Associate Member of the Science Council of Japan. He served as a vice president of JSAP from 2018−2020. He was the recipient of JSPS Award in 2005, IEEE/LEOS Distinguished Lecturer Award in 2006/2007, Ichimura Academic Award in 2012, and Education, Culture, Sports, Science Minister's Commendation in 2016